Optimized Denoising Method for Weak Acoustic Emission Signal in Partial Discharge Detection

Qingcheng Lin, Fuyong Lyu, Shiqi Yu, Hui Xiao, and Xuefeng Li, *Member, IEEE*

***Abstract*— Acoustic emission (AE) technology can predict the occurrence of partial discharge (PD) faults, which is used to improve the safe operation level of gas-insulated switchgear (GIS) equipment. However, the strong noise interference from the production site is still the main factor affecting the identification accuracy. In this study, a simplified model is designed to approximate the accumulation of free metal particles on the surface of the GIS internal insulation structure, and white noise of various intensities is added to the collected PD-induced AE signals to simulate the background interference. The results prove that the proposed denoising method can achieve a better denoising effect in various signal-to-noise ratio (SNR) conditions. In particular, in the case of low SNR, the recognition accuracy of the accumulation degree of metal particles has been improved by more than 15%.**

***Index Terms*— Denoising, gas-insulated switchgear (GIS), partial discharge (PD), pattern recognition, wavelet threshold function.**

I. Introduction

SINCE the mid-1960s, gas-insulated switchgear (GIS) has been widely used in high-voltage power transmission systems [1]. In the beginning, it was generally considered to be a maintenance-free device or, at worst, in an exceptionally long maintenance interval [2]. However, in recent decades, frequent insulation failures have become one of the most important factors that affect the reliability of GIS [3]–[5]. It is known that during the production, manufacture, and transport of GIS, the generation of structural and material defects is the main causes of insulation failures, including free metal particles, high-voltage conductor spikes, floating electrodes, insulator surface contamination, and internal defects [6]. At present, the diagnosis of GIS in factory tests and normal operations primarily relies on the monitoring of partial discharge (PD) events. Researchers focus on the early detection of PD-induced physical/chemical signals, which will track and judge the progress of insulation defects, schedule maintenance in time, and ultimately avoid serious failures [7]–[9].

It is well known that the PD process is accompanied by a variety of detectable phenomena, such as high-frequency voltage/current pulses, electromagnetic waves, light, sound, and decomposed gases. Correspondingly, different measurement methods are classified in terms of sensors (parameters), mainly including electrical detection, electromagnetic detection, optical detection, acoustic detection, and chemical detection [5]. Among them, acoustic detection techniques have many advantages, such as supporting *in situ* measurement, anti-electromagnetic interference, and independent of the capacitance of the measured object, and are widely used in the defect diagnosis of GIS during normal operation. In terms of working principle, the PD that occurs in GIS can be understood as a microexplosion that excites the emission of acoustic pressure waves, which propagate through the insulation materials and are acquired by acoustic emission (AE) sensors on the external walls of GIS [7]. Typically, high-performance piezoelectric sensors and fiber optical sensors are used to collect the AE signals, which are important because the signal quality can seriously affect the analysis results [10]. Even better, some advanced sensors and detection systems are constantly being proposed. For example, Ma *et al.* [11] proposed a novel online monitoring system for GIS based on the surface-acoustic-wave temperature sensor, which has an excellent insulation level, anti-interference ability, and monitoring performance. In addition, many researchers also focus on noise suppression, feature extraction, and pattern recognition [12], [13]. In particular, noise suppression can restore high-quality signals, which is the basis for effectively extracting AE signal features and a guarantee for accurate identification of PD faults [14].

Many studies have shown that the signals collected by sensors usually have a low signal-to-noise ratio (SNR) due to various background noises, especially the white noise interference, in the operating environment of GIS. Generally, noise suppression is achieved by processing in the time domain (adaptive filter), frequency domain (fast Fourier transform), or time–frequency domain (wavelet transform) [7]. Some new methods have also been proposed, such as singular value

Manuscript received 6 December 2021; accepted 9 April 2022. Date of publication 16 June 2022; date of current version 4 August 2022. This work was supported in part by the National Natural Science Foundation of China under Grant 62175187; in part by the Shanghai Municipal Science and Technology Major Project under Grant 2021SHZDZX0100; in part by the Shanghai Municipal Commission of Science and Technology Project under Grant 19511132101; and in part by the Key Laboratory of Optoelectronic Devices and Systems, Ministry of Education and Guangdong Province. *(Qingcheng Lin and Fuyong Lyu contributed equally to this work.) (Corresponding author: Xuefeng Li.)*

Qingcheng Lin, Fuyong Lyu, Shiqi Yu, and Hui Xiao are with the College of Electronic and Information Engineering, Tongji University, Shanghai 201804, China.

Xuefeng Li is with the College of Electronic and Information Engineering, Tongji University, Shanghai 201804, China, and the Frontiers Science Center for Intelligent Autonomous Systems, Tongji University, Shanghai 201210, China, and also with the Key Laboratory of Optoelectronic Devices and Systems, Ministry of Education and Guangdong Province, College of Physics and Optoelectronic Engineering, Shenzhen University, Shenzhen 518060, China (e-mail:lixuefeng@tongji.edu.cn).

Color versions of one or more figures in this article are available at https://doi.org/10.1109/TDEI.2022.3183662.

Digital Object Identifier 10.1109/TDEI.2022.3183662

decomposition and artificial neural network [15]. On-site detection of GIS often requires a balance between achieving better results and the minimum time lag, so the wavelet denoising has become one of the most widely used methods due to its good denoising effect and fast calculation speed [5], [10]. For the case where the signal is mixed with white noise, the wavelet multiscale analysis can shape the local characteristics of the signal in both the time domain and frequency domain, thereby greatly suppressing the noise, while well preserving the features that reflect the real signals. Therefore, this method is particularly suitable for denoising of nonstationary signals, such as PD-induced AE signals, which has been validated many times [16], [17].

The wavelet denoising refines the noisy signal stepwise at multiple scales by the telescopic translation operations, decomposes it with a suitable wavelet basis function, thresholds the wavelet coefficients to remove noise-related coefficients while preserving the coefficients required to describe the signal, and then reconstructs the signal. In this research direction, Donoho [18] first proposed the classical soft threshold function and hard threshold function, which are simple and effective and have received widespread attention. However, these two thresholding methods still have some shortcomings and limitations. For example, the hard threshold function generates additional oscillations and jump points during signal reconstruction, which cannot maintain the smoothness of the original signal. The soft threshold function compresses the signal and directly affects the approximation degree between the reconstructed signal and the real signal. Therefore, many scholars have proposed specific solutions and improvement methods [19]–[22]. These methods have shown good denoising effects in some simulated and collected signals. However, PD-induced AE waves propagate within GIS, normally in the form of damped oscillations at the detection point. In actual detection, the SNR of the collected signal is often lower than the estimated one, which leads to a sharp drop in the performance of these denoising methods and affects the accuracy of fault analysis.

In this study, an improved wavelet threshold function is newly proposed, which has the characteristics of a good noise reduction effect, low distortion, and simplicity. Comparative analyses show that the proposed noise suppression scheme combined with a suitable pattern recognition algorithm can effectively improve the recognition accuracy of the accumulation state of free metal particles on the surface of the internal insulation structures under different interference noises, especially for low SNR signals.

II. New Threshold Function

Due to the influence of GIS working environment, the white noise inevitably exists in the signals collected by the sensor, which is detrimental to the subsequent feature extraction and pattern recognition. Therefore, in practical applications, noise reduction of the collected signal is generally the first step. Currently, as shown in Fig. 1, many kinds of research are based on the decomposition of the noise-contaminated signals in the wavelet domain, and compressing or nonlinearly processing the noise with an appropriate threshold function to achieve denoising. Among them, the classical hard and soft threshold functions are the most widely used, and their function expressions are shown in the following equations [18]:

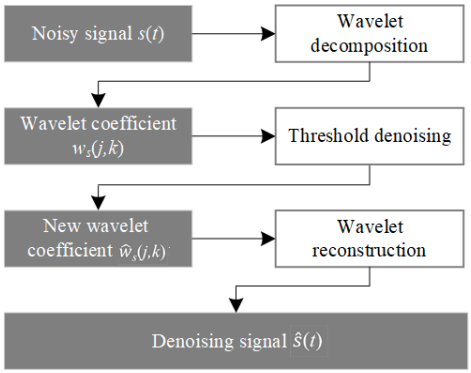

Fig. 1. Wavelet threshold function denoising process.

$$\hat{w}_s(j,k) = \begin{cases} w_s(j,k), & |w_s(j,k)| \geq \lambda \\ 0, & |w_s(j,k)| < \lambda \end{cases} \tag{1}$$

$$\hat{w}_s(j,k) = \begin{cases} \text{sign}(w_s(j,k))(|w_s(j,k)| - \lambda), & |w_s(j,k)| \geq \lambda \\ 0, & |w_s(j,k)| < \lambda \end{cases} \tag{2}$$

where λ is the set threshold greater than 0, $w_s(j,k)$ is the wavelet coefficient of the decomposition, and $\hat{w}_s(j,k)$ is the wavelet coefficient after threshold processing.

These two methods have a good denoising effect. However, their noise reduction capabilities are insufficient in low SNR signals, especially when the signal strength is completely submerged in the background noise, similar to the noise-polluted signals in this study. The reason is that for hard thresholds, the function is discontinuous when $w_s(j,k) = \lambda$, which leads to a certain fluctuation in the reconstruction of the original signals. Compared with the hard threshold function, the soft threshold function is continuous in the domain, but when the absolute value of $w_s(j,k)$ is greater than λ, there will be a constant between $\hat{w}_s(j,k)$ and $w_s(j,k)$, which will affect the accuracy of the reconstructed signals. To overcome the shortcomings, ensure the continuity of the function, and improve the constant deviation between $\hat{w}_s(j,k)$ and $w_s(j,k)$, this study uses the convexity of the exponential function to reconstruct a new threshold function based on the expression of the hard threshold function and soft threshold function, whose expression is shown in the following equation:

$$\hat{w}_s(j,k) = \begin{cases} w_s(j,k) - 0.5 \cdot \dfrac{\lambda^{m+1}}{w_s(j,k)^m}, & w_s(j,k) > \lambda \\ 0.5 \cdot \dfrac{\text{sign}(w_s(j,k)) \cdot (\text{sign}(w_s(j,k)) \cdot w_s(j,k))^{m+1}}{\lambda^m}, & |w_s(j,k)| \leq \lambda \\ w_s(j,k) + 0.5 \cdot \dfrac{\lambda^{m+1}}{(-w_s(j,k))^m}, & w_s(j,k) < -\lambda \end{cases} \tag{3}$$

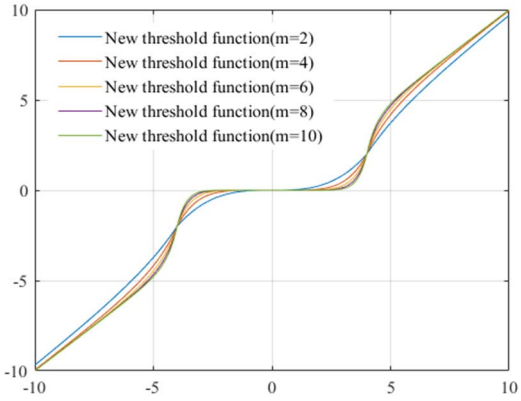

Fig. 2. Comparison on the new threshold function with different settings of *m*.

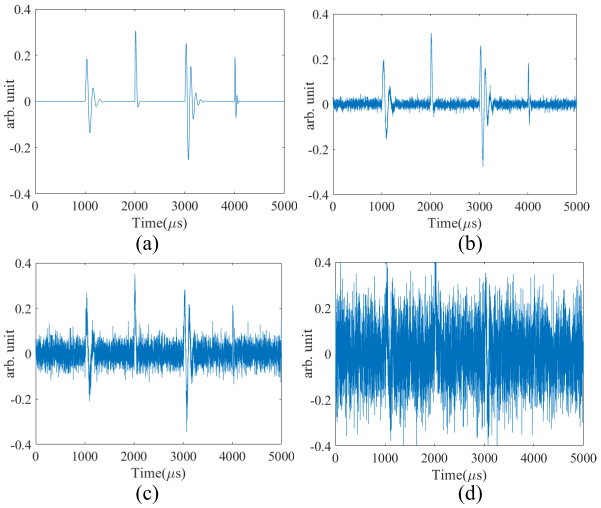

Fig. 3. Single exponentially decaying oscillation function and double exponentially decaying oscillation function are used to the simulated signals. (a) Pure signal. (b) Noisy signal with 10 dB. (c) Noisy signal with 0 dB. (d) Noisy signal with −10 dB.

where m is the adjustment coefficient of the new threshold function and is a positive integer.

Obviously, the newly constructed threshold function is continuous, namely, $\hat{w}_s(j,k)_- = \hat{w}_s(j,k)_+$, in the whole real domain. Therefore, the new threshold function improves the oscillation of signal reconstruction caused by the discontinuity of the traditional soft or hard function. Moreover, when $|w_s(j,k)| \geq \lambda$, $|\hat{w}_s(j,k) - w_s(j,k)| = 0.5 \cdot \lambda^{m+1}/w_s(j,k)^m$. Since $m \geq 1$, the constant deviation between $\hat{w}_s(j,k)$ and $w_s(j,k)$ decreases with the increase of $|w_s(j,k)|$, which improves the accuracy of signal reconstruction. In addition, m is adjustable, and for noise-polluted signals with different SNRs, the best threshold function can be obtained by adjusting the coefficients. In Fig. 2, the colored solid lines show threshold functions for different m values (2, 4, 6, 8, and 10) at $\lambda = 4$. Its impact on the noise reduction effect will be analyzed in Section III.

III. Simulation and Analysis

In this section, the proposed wavelet threshold function is compared with the classical hard, soft, and some new research results through the simulation analysis of the noise reduction effects at different SNRs.

A. Signal Samples

The double exponentially damping oscillation function y_1 and the single exponentially damping oscillation function y_2 are used to produce signals for simulation analysis, and the equations are shown in the following equations [23]:

$$y_1 = A\left(e^{\frac{-1.3t}{\tau}} - e^{\frac{-2.2t}{\tau}}\right)\sin 2\pi f_c t \tag{4}$$

$$y_2 = Ae^{\frac{-t}{\tau}}\sin 2\pi f_c t \tag{5}$$

where A is the amplitude of the signal, τ is the attenuation coefficient, and f_c is the oscillation frequency. The generated signals are shown in Fig. 3(a), which contains four different pulses to generate the diversity of samples. Here, the first and third are from (4), and the second and fourth are from (5), which are in order, A is 1.0, 0.8, 1.5, and 0.3; τ is 4.0, 1.0, 4.0, and 1.0 μs; and f_c is 150, 200, 200, and 500 kHz. Then, Gaussian white noise is added to the generated signal to construct noise-polluted signals of different SNRs of 10, 0, and −10 dB, as shown in Fig. 3(b)–(d), which are used to compare the noise reduction effect of threshold functions.

B. Comparative Analysis

As the adjustable coefficient of the proposed new threshold function, m is first evaluated. It is well known that the PD-induced AE signal is usually a damping oscillation waveform at the detection point, which is highly similar to the Daubechies wavelet. Among them, the db2 wavelet function has the highest similarity with the AE signals, exceeding 90% [24]. Therefore, a six-layer wavelet decomposition is performed on the noisy signal, and db2 is used as the wavelet basis in this study. Equation (6) is determined as the threshold value for processing the wavelet coefficients in each layer

$$\lambda = \sigma\frac{\sqrt{2\mathrm{In}N}}{\mathrm{In}(j+1)} \tag{6}$$

where $w_s(j,k)$ represents the decomposition coefficient on each scale, j represents the decomposition scale, N represents the length or the size of the signals, and σ represents the noise variance (VAR).

Here, the SNR and root-mean-square error (RMSE) are used for denoising effect evaluation. The results are shown in Fig. 4. As m increases, the SNR and RMSE of the denoised signals are improved and tend to converge. However, for noisy signals with different SNRs, different values of m are set to achieve the best denoising effect. The signal denoising effect of low SNR is better when m is greater than or equal to 6. The denoising effect of medium and high SNR signals is better when m is between 3 and 5, and the effect decreases slightly after m is greater than 6. Overall, considering that the actual AE signal acquisition process is interfered by environmental noise, which leads to a low SNR, in the subsequent simulations and experiments, m is set to 6 in this study. Moreover,

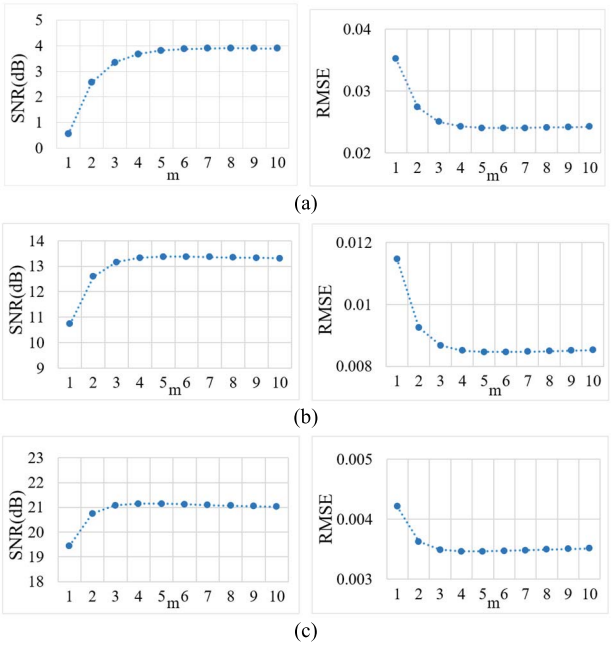

Fig. 4. SNR and RMSE change with different m's. (a) Low-SNR signal (−10 dB). (b) Medium-SNR signal (0 dB). (c) High-SNR signal (10 dB).

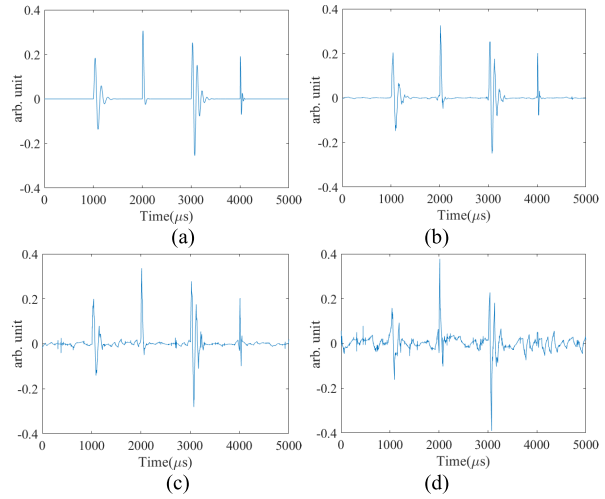

Fig. 5. Noise reduction signals were obtained based on the proposed new threshold function. (a) Pure signal. (b) Noisy signal with 10-dB SNR. (c) Noisy signal with 0-dB SNR. (d) Noisy signal with −10-dB SNR.

m can also be adjusted to obtain the best denoising effect by preevaluating the SNR of the noisy signal in practical applications.

To evaluate the effectiveness of the proposed new threshold function, simulation analyses and comparisons are carried out with the traditional hard threshold, soft threshold, and four other improved threshold functions. As shown in Table I, the noise reduction effect of the new threshold function is the best, which benefits the subsequent signal analysis. Fig. 5 shows the noise reduction results of the proposed new threshold function, which corresponds one-to-one with the signals in Fig. 3. Among them, Fig. 5(a) shows that the noise reduction processing does not damage the generated signal, that is, the pure signal without noise. Fig. 5(b) and (c) shows that with increasing noise intensity, the effect of noise reduction gradually worsens. However, for noisy signals with a high SNR (10 dB) and medium SNR (0 dB), good signal integrity can still be maintained after noise reduction. Fig. 5(d) shows that for a noisy signal with a low SNR (−10 dB), the noise reduction process causes some damage, the first three pulses are appropriately retained, and the fourth pulse cannot be observed.

TABLE I
COMPARISON OF NOISE REDUCTION EFFECTS

Noise reduction	Threshold function	SNR (dB)		
Before	-	10	0	-10
After	Soft	16.91	9.94	3.27
	Hard	20.89	13.08	4.17
	[19]	16.83	9.94	3.03
	[20]	20.77	13.23	4.35
	[21]	20.16	12.22	4.09
	[22]	18.67	11.86	4.35
	Our work	21.39	13.29	4.77

IV. EXPERIMENT AND ANALYSIS

In this section, an experimental platform is built to simulate the occurrence of PD fault induced by metal particles accumulated on the surface of the insulating structures of GIS. AE signals are collected in different discharge models, and the noise suppression effect of each wavelet threshold function is indirectly compared and evaluated through the recognition accuracy of the support vector machine (SVM).

A. Platform Construction and Signal Acquisition

The detection system used in this study is shown in Fig. 6(a), including a 15-kV high-voltage source to power the defect model; a piezoelectric AE sensor with a resonant frequency of 30 kHz and a bandwidth of 10 dB from 20 to 110 kHz, used for signal acquisition; a preamplifier with a gain of 40 dB and a bandwidth of 0.01–2.0 MHz for amplifying the output signals; and a processing terminal PC with a high-speed data acquisition card. The experimental platform and the approximate defect models are shown in Fig. 6(b) and (c), respectively. Here, the free metal particles in the defect models are simulated by copper beads with different diameters. The metal particles used in the four models are 1.0, 1.8, 2.0, and 2.5 mm in diameter, and uniformity gaps of 0.15 mm are ensured between the copper beads. The completed defect models are sequentially fixed on the surface of the insulating structure (the side close to the center conductor), forming a 5-cm-long structure. The copper beads at both ends of the channel are, respectively, in close contact with the needle of a tungsten–iron alloy (high potential terminal) and the center conductor (grounding), which form the discharge channel. Finally, a 14-kV voltage is applied to simulate the occurrence of PD failures. Simultaneously, the

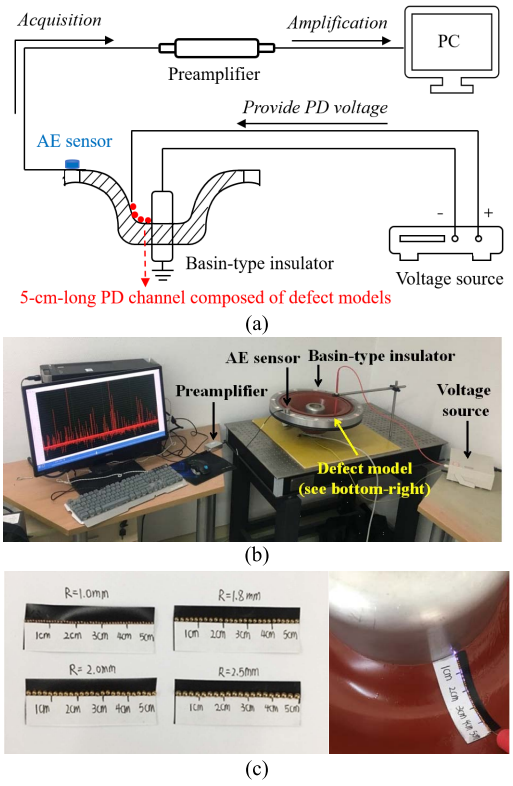

Fig. 6. Experiment of PD-induced AE signals detection. (a) Fault detection system. (b) Experimental platform. (c) Defect models.

signals are collected by the AE sensor set on the connecting interface of GIS shell.

In Fig. 7, four groups of PD-induced AE signals based on their respective defect models are shown. The periods of the PD decrease gradually, and the signal amplitudes decrease gradually with the increase of the diameter of the metal particles in the model. This is because if the gap between the copper beads is the same, the larger the projection area of the copper bead, the lower the equivalent resistance of the discharge channel, and PD is more likely to occur and stabilize. In this study, the above method is used to simulate the PD failures caused by the accumulation of free metal particles on the surface of the insulation structure, and the induced AE signals are collected.

B. Noise Addition and Noise Reduction

The purpose of designing this experiment is to verify the denoising effect of the proposed new threshold function. Therefore, white noise with different intensities is added to the above collected signals. It is worth noting that the collected original signals generally contain many noise components, including current noise, thermal noise, and vibration noise. With the damping platform and the stable experimental environment, the interferences can be reduced to a very low level compared with the GIS operating site. As shown in Fig. 7, the tiny noise components can be negligible. These collected signals are assumed to be ideal real signals in this study.

According to the simulation and analysis results in Section III, the collected signals are first processed by adding

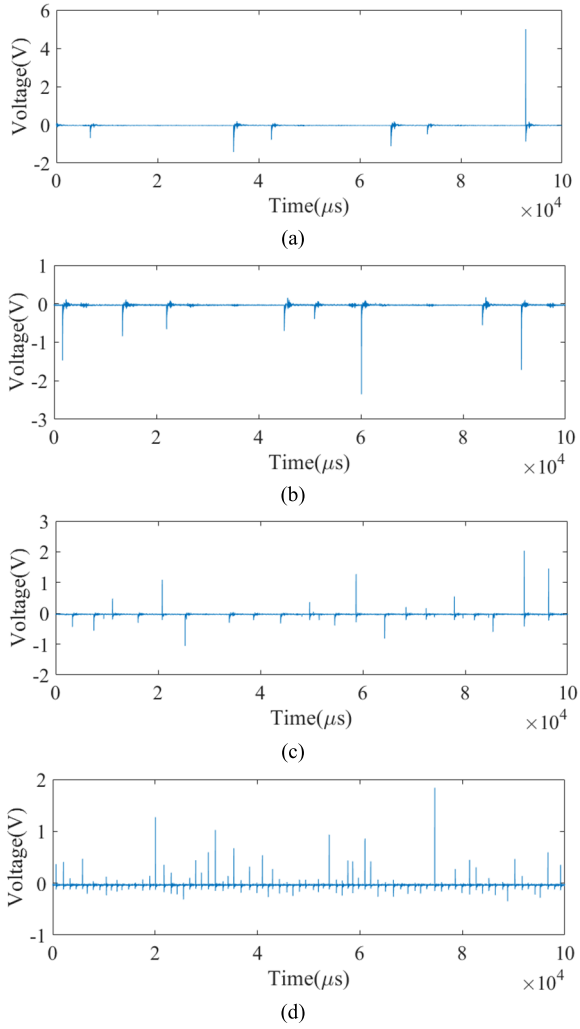

Fig. 7. PD-induced AE signals of different defect models with four metal particle diameters. (a) 1.0 mm. (b) 1.8 mm. (c) 2.0 mm. (d) 2.5 mm.

noise to obtain noisy signals with a −10-dB SNR. Comparing the induced signal of defect model 4 shown in Fig. 7(d), it can be seen that in Fig. 8(a), most of the signals have been submerged by noise, except for a few high-amplitude pulses. The reason for this is that, on the one hand, this set of AE signals contains pulses with rich differences in intensity, and on the other hand, it is easier to compare the differences in the threshold functions by analyzing the noise reduction effects of the low SNR signals. Fig. 8(b)–(h) shows the noise reduction effect of each threshold function, including the traditional soft threshold, the hard threshold, the four improved threshold functions, and the proposed new threshold function. It can be observed that the noise reduction effects in Fig. 8(c), (e), and (h) are better in terms of noise suppression and signal retention. Their graphs are very similar, but more tiny bumps are shown in Fig. 8(h), which requires further analysis to determine whether it is helpful for the identification of PD faults. Because the experimentally collected PD-induced AE signals themselves contain tiny noises, and the denoising effects are not suitable for direct comparison by SNR. Here, the AE signals of four defect models are collected, noise

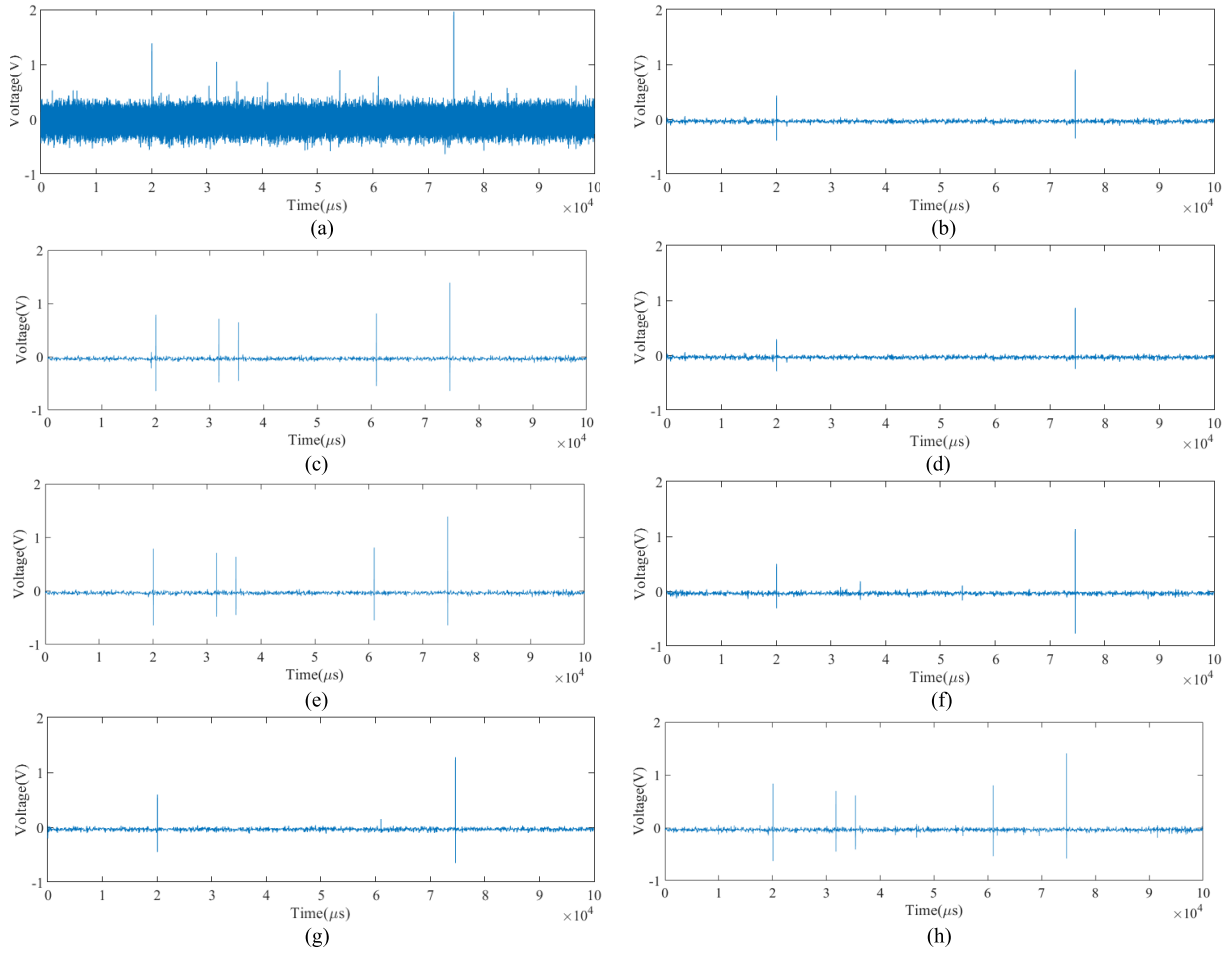

Fig. 8. Noise-polluted signal and its noise reduction signals are obtained based on each threshold function. (a) Noisy signal with −10-dB SNR. (b) Noise reduction with soft threshold function. (c) Hard threshold function. (d) Threshold function from [19]. (e) Threshold function from [20]. (f) Threshold function from [21]. (g) Threshold function from [22]. (h) New threshold function of our work.

is added, noise reductions are applied, and each noise suppression effect is indirectly compared through the recognition accuracy of SVM.

C. Pattern Recognition

The purpose of designing this experiment is to further verify the denoising effect of the proposed new threshold function. Therefore, white noise with different intensities is added to the above collected signals. In this study, the accumulation states of free metal particles are used as the identification target. First, based on the experimental platform, PD-induced AE signals are continuously collected for 200 s in each defect model as original signal data. Then, these signals are polluted with white noise to construct four groups of arithmetic sequence signals with SNRs ranging from −20 to 10 dB. Finally, each group of noisy signals is segmented with a step size of 1.0 s to construct a dataset with four types of faults and 800 vectors. In this way, four groups of signals with different SNRs constitute four datasets. Next, nine features are extracted from the 1.0-s signal to construct the eigenvalue vector, including the root mean square (rms), VAR, standard deviation (SD), waveform factor (WF), kurtosis (K), and skewness (SK) in the time domain; and the maximum power spectrum (MPS), integration of power spectral density (IPSD), and mean power frequency (MPF) in the frequency domain. Then, the feature vectors are randomly selected in each dataset, 90% as the training set and 10% as the test set. This random selection process is repeated ten times, and the average of the recognition accuracies is used as the final evaluation results.

In practical applications, the appropriate algorithm is usually selected according to the characteristics of the data type and the size of the dataset. Therefore, SVM, which is suitable for small sample learning, is used to classify and identify PD fault types in this study. A Gaussian function with good adaptability and versatility is selected as the kernel function, also known as the radial basis function (RBF), which is the most commonly used kernel function for SVM. It is important to note that the choice of the two hyperparameters, namely, the parameter g of the RBF kernel function and the penalty factor C, is very important. Specifically, when C is too large, the classifier is easy to overfit, and when C is too small, the classifier is easy to underfit, which affects the generalization ability of the algorithm. g determines the complexity of the SVM classification algorithm. If it is too large, it will lead to overfitting, and if it is too small, it will lead to underfitting.

TABLE II
RECOGNITION ACCURACIES OF DIFFERENT THRESHOLD FUNCTIONS WITH DIFFERENT SNRS

Threshold function	SNR before noise reduction (dB)			
	10	0	-10	-20
Average recognition accuracy (%)				
Soft	86.25	89.63	88.38	39.50
Hard	92.75	87.50	90.38	45.00
[19]	93.75	88.00	88.88	41.50
[20]	90.13	88.13	86.88	35.50
[21]	91.75	88.50	86.75	38.13
[22]	91.88	88.50	89.88	39.25
Our work	**93.88**	**91.63**	**91.25**	**60.88**
Standard deviation				
Soft	0.044	0.021	0.034	0.055
Hard	0.027	0.044	0.027	0.024
[19]	0.032	0.029	0.042	0.033
[20]	0.030	0.013	0.027	0.043
[21]	0.038	0.030	0.028	0.045
[22]	0.043	0.020	0.037	0.053
Our work	0.027	0.010	0.030	0.029

Both are the keys to affecting the performance of SVM classifier and they are optimized using k-fold cross-validation (K-CV) and the grid search (GS) methods [25].

As described in Section III, the comparisons are based on the noise signals with low, medium, and high SNRs of −10, 0, and 10 dB, respectively. In addition, a noise signal with a worse SNR of −20 dB is further added to analyze the noise reduction effect under extreme conditions. Table II shows that denoising with the new threshold function outperforms all other functions and is the only indication that all the three groups of signals with low, medium, and high SNRs are identified with an accuracy above 90%. This is the same situation as observed in Fig. 8, which has the best results in terms of noise suppression and signal retention. At low-quality signals with −20-dB SNR, the recognition accuracy using the new threshold function drops to approximately 60%, which is still low, although it shows a greater advantage of at least 15% over the others. The purpose of adding noise to the collected signal in this section is to verify the effectiveness of the noise reduction algorithm. The noisy signal with −20-dB SNR is a difficult challenge. It is necessary to optimize and combine other links such as feature extraction and pattern recognition to improve the recognition accuracy in subsequent research.

V. CONCLUSION

The core contribution of this work is to design a new threshold function for wavelet denoising, which can achieve a better denoising effect in various SNRs. The results show that the proposed denoising method effectively improves the recognition accuracy of the accumulation state of free metal particles on the surface of the internal insulation structure, which has been even improved by more than 15% in the case of low SNR. The overall solution has a universal reference value for online monitoring and research on the PD phenomena of GIS and other metal-enclosed equipment and can provide necessary technical support for the monitoring and operation of high-voltage power supply systems.

However, this study also has some limitations. All the AE signals analyzed are from the simplified model of "accumulation state of free metal particles on the surface of internal insulation structures," which is not completely consistent with the structure of the actual GIS equipment. For example, the interior of GIS is filled with high-pressure SF_6 gas, and the free metal particles on the surface of insulating structure are disorganized. The validity of the noise reduction algorithm for AE signals induced by other types of faults and the application ability of on-site detection needs to be further verified. These works will continue to be studied in the follow-up work.

ACKNOWLEDGMENT

Collected acoustic emission (AE) signals and extracted dataset can be downloaded at https://u.pcloud.link/publink/show?code = kZ9oGUXZTHwL6aXeNXjaVsq07E45uhW5V-Jqk (extraction code: LIGHTING601), provided by the authors.

REFERENCES

[1] S. Okabe, G. Ueta, H. Hama, T. Ito, M. Hikita, and H. Okubo, "New aspects of UHF PD diagnostics on gas-insulated systems," *IEEE Trans. Dielectr. Electr. Insul.*, vol. 21, no. 5, pp. 2245–2258, Oct. 2014.
[2] A. Darwish, S. S. Refaat, H. Abu-Rub, and H. A. Toliyat, "PD signal propagation in GIS: Ultra-high frequency detection-based modeling," *IEEE Sensors J.*, vol. 20, no. 16, pp. 9417–9426, Aug. 2020.
[3] S. Zheng and S. Wu, "Detection study on propagation characteristics of partial discharge optical signal in GIS," *IEEE Trans. Instrum. Meas.*, vol. 70, pp. 1–12, 2021.
[4] Z. Zhang *et al.*, "Research on partial discharge state detection in GIS based on Internet of Things technology," *J. Phys. Conf.*, vol. 1549, no. 4, Jun. 2020, Art. no. 042012.
[5] Q. Khan, S. S. Refaat, H. Abu-Rub, and H. A. Toliyat, "Partial discharge detection and diagnosis in gas insulated switchgear: State of the art," *IEEE Elect. Insul. Mag.*, vol. 35, no. 4, pp. 16–33, Jul./Aug. 2019.
[6] B. Qi *et al.*, "Partial discharge initiated by free moving metallic particles on GIS insulator surface: Severity diagnosis and assessment," *IEEE Trans. Dielectr. Electr. Insul.*, vol. 21, no. 2, pp. 766–774, Apr. 2014.
[7] H. D. Ilkhechi and M. H. Samimi, "Applications of the acoustic method in partial discharge measurement: A review," *IEEE Trans. Dielectr. Electr. Insul.*, vol. 28, no. 1, pp. 42–51, Feb. 2021.
[8] Y. Gao, H. Wang, X. Yuan, H. Zhao, and Z. Li, "Surface charge accumulation on a real size epoxy insulator with bouncing metal particle under DC voltage," *IEEE Trans. Plasma Sci.*, vol. 49, no. 7, pp. 2166–2175, Jul. 2021.
[9] H. You *et al.*, "Motion and discharge characteristics of metal particles existing in GIS under DC voltage," *IEEE Trans. Dielectr. Electr. Insul.*, vol. 24, no. 2, pp. 876–885, Apr. 2017.
[10] I. Bua-Nunez, J. E. Posada-Roman, J. Rubio-Serrano, and J. A. Garcia-Souto, "Instrumentation system for location of partial discharges using acoustic detection with piezoelectric transducers and optical fiber sensors," *IEEE Trans. Instrum. Meas.*, vol. 63, no. 5, pp. 1002–1013, May 2014.
[11] G. M. Ma *et al.*, "A wireless and passive online temperature monitoring system for GIS based on surface-acoustic-wave sensor," *IEEE Trans. Power Del.*, vol. 31, no. 3, pp. 1270–1280, Jun. 2016.
[12] M. Kunicki, "Analysis on acoustic disturbance signals expected during partial discharge measurements in power tansformers," *Arch. Acoust.*, vol. 45, no. 4, pp. 733–746, 2020.

[13] Y.-B. Wang *et al.*, "Acoustic localization of partial discharge sources in power transformers using a particle-swarm-optimization-route-searching algorithm," *IEEE Trans. Dielectr. Electr. Insul.*, vol. 24, no. 6, pp. 3647–3656, Dec. 2017.
[14] X. Peng *et al.*, "SDMF based interference rejection and PD interpretation for simulated defects in HV cable diagnostics," *IEEE Trans. Dielectr. Electr. Insul.*, vol. 24, no. 1, pp. 83–91, Feb. 2017.
[15] X. Yang, H. Huang, Q. Shu, D. Zhang, and B. Chen, "Partial discharge signal extraction method based on EDSSV and low rank RBF neural network," *IEEE Access*, vol. 9, pp. 9744–9752, 2021.
[16] X. Ma, C. Zhou, and I. J. Kemp, "Automated wavelet selection and thresholding for PD detection," *IEEE Electr. Insul. Mag.*, vol. 18, no. 2, pp. 37–45, Mar. 2002.
[17] J. Seo, H. Ma, and T. Saha, "Probabilistic wavelet transform for partial discharge measurement of transformer," *IEEE Trans. Dielectr. Electr. Insul.*, vol. 22, no. 2, pp. 1105–1117, Apr. 2015.
[18] D. L. Donoho, "De-noising by soft-thresholding," *IEEE Trans. Inf. Theory*, vol. 41, no. 3, pp. 613–627, Mar. 1995.
[19] R.-M. Zhao and H.-M. Cui, "Improved threshold denoising method based on wavelet transform," in *Proc. 7th Int. Conf. Model., Identificat. Control (ICMIC)*, Dec. 2015, pp. 1–4.
[20] L. Jing-Yi, L. Hong, Y. Dong, and Z. Yan-Sheng, "A new wavelet threshold function and denoising application," *Math. Problems Eng.*, vol. 2016, pp. 1–8, Apr. 2016.
[21] C. He, J. Xing, J. Li, Q. Yang, and R. Wang, "A new wavelet thresholding function based on hyperbolic tangent function," *Math. Problems Eng.*, vol. 2015, pp. 1–10, Nov. 2015.
[22] Y. Wang, B. Zhang, F. Ding, and H. Ren, "Estimating dynamic motion parameters with an improved wavelet thresholding and inter-scale correlation," *IEEE Access*, vol. 6, pp. 39827–39838, 2018.
[23] B. Raghavendra and M. K. Chaitanya, "Comparative analysis and optimal wavelet selection of partial discharge de-noising methods in gas-insulated substation," in *Proc. 3rd Int. Conf. Adv. Electr., Electron., Inf., Commun. Bio-Inform. (AEEICB)*, Feb. 2017, pp. 1–5.
[24] J. Zhang, H. Zhou, and P. Zhou, "New de-noising method for partial discharge signals based on wavelet threshold," *Adv. Techno. Elec. Eng. Energy.*, vol. 36, no. 8, pp. 80–88, Aug. 2017.
[25] X. Gao and J. Hou, "An improved SVM integrated GS-PCA fault diagnosis approach of Tennessee Eastman process," *Neurocomputing*, vol. 174, pp. 906–911, Oct. 2016.

Qingcheng Lin received the B.S. degree in mechanical design and manufacturing and automation from Northeastern University, Shenyang, China, in 2018. She is currently pursuing the Ph.D. degree in control theory and control engineering with the Department of Control Science and Engineering, Tongji University, Shanghai, China.

Her research interests include machine learning and intelligent control.

Fuyong Lyu received the B.S. degree from Tongji University, Shanghai, China, in 2019, where he is currently pursuing the M.S. degree in control theory and control engineering with the Department of Control Science and Engineering.

His research interests are in optical fiber sensor development and detection technology.

Shiqi Yu received the B.S. degree from the Xi'an University of Architecture and Technology, Xi'an, China, in 2019. She is currently pursuing the M.S. degree in control theory and control engineering with the Department of Control Science and Engineering, Tongji University, Shanghai, China.

Her research interests are in sensors and modeling.

Hui Xiao received the B.S., M.S., and Ph.D. degrees in control theory and control engineering from the Department of Control Science and Engineering, Tongji University, Shanghai, China, in 1992, 1998, and 2007, respectively.

She was a Lecturer and an Associate Professor with Tongji University from 1992 to 1997 and 1997 to 2011, respectively, where she has been a Professor since 2011. Her research interests are in intelligent building, intelligent control, life optics, and novel application techniques.

Xuefeng Li (Member, IEEE) received the degree from the Shenyang Institute of Engineering, Shenyang, China, in 1999, and the M.S. and Ph.D. degrees from the Fukuoka Institute of Technology, Fukuoka, Japan, in 2004 and 2007, respectively.

From 2007 to 2013, he was a Post-Doctoral Researcher and an Assistant Researcher with Waseda University, Kitakyushu, Japan. Since 2013, he has been an Associate Professor with Tongji University, Shanghai, China. From 2022 to 2023, he is being employed as a visiting researcher in the Key Laboratory of Optoelectronic Devices and Systems, Ministry of Education and Guangdong Province, Shenzhen University. His research interests include intelligence and information processing.